Deep-UV Photonic Crystal Surface-Emitting Lasers

LASER & PHOTONICS REVIEWS
www.lpr-journal.org

Deep-UV Photonic Crystal Surface-Emitting Lasers

Doğukan Apaydın, Hjalmar Andersson, Lukas Uhlig, Sarina Graupeter, Joachim Ciers, Giulia Cardinali, Erik Strandberg, Tim Wernicke, Michael Kneissl, Ulrich Theodor Schwarz, Philippe Tassin, and Åsa Haglund*

Today's ultraviolet lasers are bulky, expensive, have low power-conversion efficiency, and usually suffer from poor beam quality. Semiconductor lasers have addressed these issues in the visible and infrared parts of the electromagnetic spectrum; but in the ultraviolet, they are just starting to see the light of day. Edge-emitting semiconductor lasers are the only ones demonstrated under electrical injection in the deep-ultraviolet (λ<280 nm) and they inherently suffer from poor beam qualities, multiple modes, and catastrophic optical damage to the mirror. The first deep-UV photonic crystal surface-emitting lasers are demonstrated here. The devices show single-mode emission around 279 nm with less than 1° beam divergence. They require a specific design to overcome optical scattering and the low refractive index that otherwise prohibits a 2D standing optical field. The optically pumped deep-ultraviolet photonic crystal surface-emitting lasers offer drastically improved beam quality and provide an important step toward low-divergent, watt-class, electrically-driven UV PCSELs.

1. Introduction

Semiconductor lasers have revolutionized many fields with their ability to deliver coherent light from a small volume in a power-efficient way. They have therefore become the light source of choice for many applications in optical communication,[1] metrology,[2] and spectroscopy.[3] Different laser types have been developed to satisfy different needs, where an edge-emitting laser (EEL)[4] can deliver high optical output power but with an elliptical output beam, and a vertical-cavity surface-emitting laser (VCSEL)[5] can deliver a circularly symmetric low-divergent beam but with low output powers in a single mode. More recently, a new type of semiconductor laser has emerged: the photonic crystal surface-emitting laser (PCSEL), which offers the potential to overcome this trade-off between output power and beam quality in traditional laser diodes.[6] A PCSEL[7] is from an epitaxial point of view similar to an EEL, but with a 2D photonic crystal integrated either on top of or below the active region. The photonic crystal results in a photonic band structure where the group velocity of light goes to zero at the band edges.[8] At these wavelengths, a 2D standing optical field can be formed and lasing can be achieved. Surface emission is then realized by out-of-plane diffraction of the mode with zero group velocity at the photonic band edges.

The first demonstration of lasing from a photonic crystal surface-emitting laser was achieved in 1999.[9] This concept has since been applied to different material systems and enabled the development of high-power laser diodes at various wavelengths. Infrared PCSELs have reached an output power of 50 W under continuous-wave operation in a single mode with a divergence angle below 0.05°.[10] Blue PCSELs were demonstrated in 2008,[11] but it was not until 2022 that they reached watt-level output powers,[12] while green-emitting PCSELs have recently been demonstrated under pulsed operation with tens of mW in output power.[13]

There is a strong interest in pushing the emission wavelength of semiconductor lasers to much shorter wavelengths, into the ultraviolet (UV) spectrum, but this has proven to be challenging. The first deep-UV, i.e., UV-C (<280 nm) EEL under continuous-wave electrical injection[14] and the first UV-B (280–320 nm) EEL under pulsed electrical injection[15] were recently demonstrated, while VCSELs have only been demonstrated under pulsed optical

D. Apaydın, J. Ciers, E. Strandberg, Å. Haglund
Department of Microtechnology and Nanoscience
Chalmers University of Technology
Gothenburg 41296, Sweden
E-mail: apaydin@chalmers.se

H. Andersson, P. Tassin
Department of Physics
Chalmers University of Technology
Gothenburg 41296, Sweden

L. Uhlig, U. T. Schwarz
Institute of Physics
Chemnitz University of Technology
09126 Chemnitz, Germany

S. Graupeter, G. Cardinali, T. Wernicke, M. Kneissl
Institute of Solid State Physics
Technische Universität Berlin
10623 Berlin, Germany

M. Kneissl
Ferdinand-Braun-Institut
12489 Berlin, Germany

[Correction added on 25 October 2025, after first online publication: the ninth author's affiliation has been updated in this version.]

DOI: 10.1002/lpor.202500271

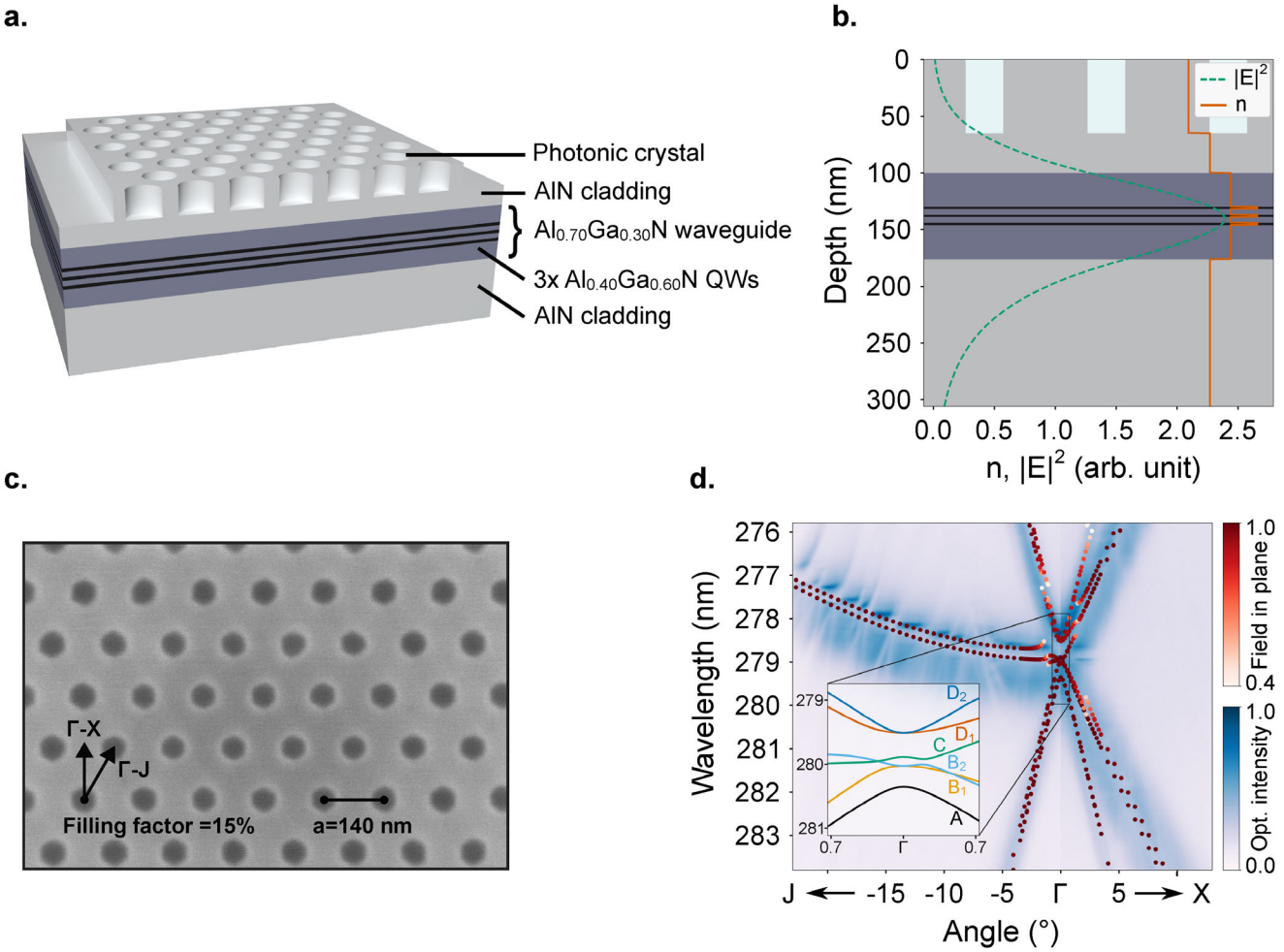

Figure 1. a) Schematic view of the PCSEL. b) Horizontally averaged refractive index profile (orange, solid line) and vertical mode intensity profile (green, dashed line) for mode B_1 at the Γ-point. c) A zoomed-in top-view scanning electron microscope image of the dry-etched photonic crystal after resist removal. d) Measured (blue color scale) and calculated (red dots) band structure along Γ-J and Γ-X directions for a PCSEL with a period of 140 nm, an etch depth of 65 nm, and a hole-filling factor of 15%. The inset shows the calculated band structure close to the Γ-point with labeling of the six transverse electric modes. Modes A, B_1, B_2, C, D_1, and D_2 are labeled in ascending order at the Γ-point, where B_1, B_2 and D_1, D_2 are degenerate.

pumping in the UV-B[16] and UV-C.[17,18] In the UV-C range, random lasing action has been achieved with AlGaN nanowires under electrical injection.[19] When it comes to UV lasers employing 2D photonic crystals, there is one report on a continuous-wave electrically-injected laser with a nanowire-based photonic crystal emitting at 367 nm, i.e., in the UV-A (320–400 nm).[20] However, it is not shown that lasing occurs at a band edge, which is often used to confirm lasing set by a 2D photonic crystal.[21]

A big challenge in realizing UV PCSELs is the difficulty in achieving 2D oscillation due to the low refractive index of AlGaN materials, which results in a weak 2D coupling.[12] In addition, this already low 2D coupling can be further deteriorated by an increased optical scattering at these short wavelengths that is caused by a stronger influence from surface roughness and small geometrical deviation from the perfect lattice.

Here, we demonstrate the first PCSELs emitting at deep-UV wavelengths under optical pumping. With the appropriate design and fabrication process, it is possible to achieve the high-quality factor needed to achieve lasing. By choosing the correct hole-filling factor, we enforce the laser to operate at a mode with low lateral loss, which produces the desired low-divergent (<1°) far-fields.

2. Results

2.1. Device Structure and Fabrication

A schematic of the PCSEL is shown in **Figure 1a**. The epitaxial structure was grown by metal organic vapor-phase epitaxy on a high-temperature annealed AlN/sapphire template.[22] It consists of a 1000-nm-thick AlN cladding, followed by a 30-nm-thick $Al_{0.70}Ga_{0.30}N$ waveguide, three 2-nm-thick $Al_{0.40}Ga_{0.60}N$ quantum wells (QW) with 5-nm-thick $Al_{0.70}Ga_{0.30}N$ barriers, and a top 30-nm-thick $Al_{0.70}Ga_{0.30}N$ waveguide layer with a 100-nm-thick AlN top cladding layer. The hexagonal photonic crystal with a period of 140 nm and a lateral size of 140 x 140 μm^2 was defined by e-beam lithography and dry etched 65 nm deep into the top AlN cladding using Cl_2/Ar plasma etching. The full process flow is

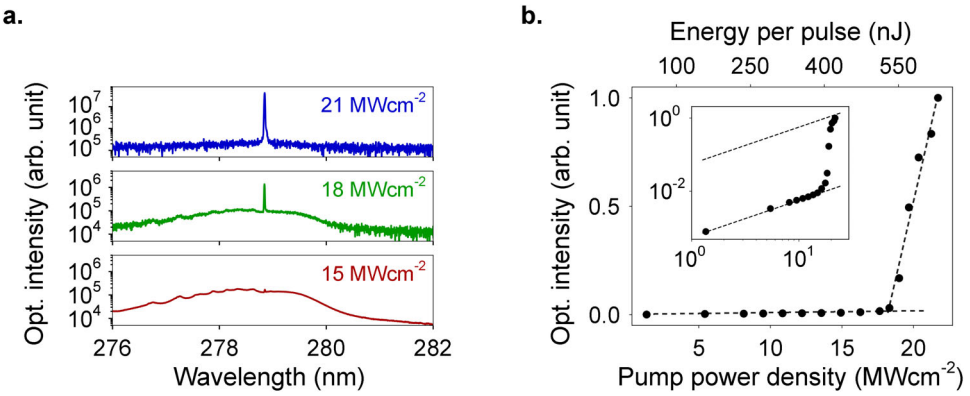

Figure 2. a) Photoluminescence spectra in logarithmic scale at room temperature for different pump power densities under pulsed optical pumping. b) The optical output intensity integrated over ±40 pm around the lasing wavelength at room temperature as a function of pump power density and energy per pulse. The inset shows a double logarithmic plot of the same data.

described in Figure S1 (Supporting Information). This left a distance of 65 nm to the topmost QW, which is enough to avoid a reduction of the internal quantum efficiency due to plasma-induced damage to the QWs.[23–25] The main advantage of this approach is that it eliminates the need for regrowth which significantly simplifies the fabrication process and avoids the risk of degrading the active region when the growth fronts merge above the photonic crystal shortly before the QWs during regrowth.

The vertical waveguide structure is designed such that the maximum of the mode distribution is aligned with the QWs and a tail of the mode overlaps with the photonic crystal on top, as shown in Figure 1b. For a hole-filling factor of 15%, this gives a confinement factor of $\Gamma_{QW} = 6.7\%$ in the QWs and $\Gamma_{PC} = 2.9\%$ in the photonic crystal layer for the B_1 mode. The filling factor represents the ratio of the area occupied by the air hole to the unit cell area. A high Γ_{QW} is important for high modal gain, while a high Γ_{PC} is crucial for strong in-plane feedback.[12]

As a result, the investigated square lattices did only show lasing through 1D oscillation and the focus was therefore turned to using a hexagonal lattice instead. Circular holes were used to minimize vertical losses and thereby the lasing threshold through nonradiating bound-state-in-the-continuum modes.[26,27] We fabricated a large number of devices with different hole diameters leading to filling factors ranging from 10% to 22%. Figure 1c shows a top-view scanning electron microscope image of a PCSEL with a hole-filling factor of 15%. In Figure 1d, we show an excellent agreement between the measured and simulated band structure along the Γ-J and Γ-X directions for a PCSEL with a period of 140 nm, an etch depth of 65 nm, and a 15% hole-filling factor. In the inset, we show the relevant bands around the Γ-point, where the modes have vanishing group velocity. It is this vanishing group velocity that creates the confinement of light necessary for lasing action to occur. We refer to the Methods Section for more details on the measurement setup and simulation methods.

2.2. Lasing Threshold and Emission Spectrum

Figure 2a shows the spectra of a PCSEL with a filling factor of 15% at different pump power densities. At 17 MWcm^{-2}, the PCSEL has a broadband spontaneous emission centered at 278.4 nm with a spectral full width at half maximum (FWHM) of approximately 2.3 nm. With increasing pump power density, the linewidth undergoes significant reduction and a 17-pm-narrow lasing peak (resolution limit set by the spectrometer) starts to appear at 278.85 nm for pump power densities above 17 MWcm^{-2}. Up to the maximum pump power density of 21 MWcm^{-2}, which is set by the maximum pump power available from the pump laser and the pump spot size, the peak intensity steeply increases with increasing pump power density and the PCSEL stays single mode.

In Figure 2b, we show the output intensity integrated over ± 40 pm around the lasing peak as a function of the pump power density under pulsed optical pumping. For a pump spot size of 82 μm FWHM, aligned to the center of the 140 x 140 μm^2-sized PCSEL, the PCSEL exhibits distinct threshold behavior around 17 MWcm^{-2}. It is worth mentioning that about 20% of the pump beam is reflected by the photonic crystal and of the remaining intensity only about 5% is absorbed by the QWs. Thus, the effective threshold pump power density is much lower than the stated value.

2.3. Photonic Band Structure

Figure 3 shows angle-resolved emission spectra below and above threshold for three PCSELs with a lattice constant of 140 nm and different photonic crystal hole radii (24, 29, and 34 nm). These radii correspond to hole-filling factors of 10%, 15%, and 22%, respectively. All devices show similar band structures below threshold (recorded along the Γ-J direction) matching the simulations in Figure 1d. The bands exhibit a slight shift toward shorter wavelengths of the Γ-point modes with increasing filling factor. This is due to a reduced effective refractive index of the photonic crystal layer with increasing filling factor caused by an increased air-to-material ratio. As a result, the mode's vacuum wavelength at the Γ-point shifts toward shorter wavelengths to compensate for this decrease in average refractive index.

Above threshold, a single lasing peak is achieved for all filling factors. The magnified views of the lasing peaks are depicted as insets. However, lasing occurs in different Γ-point modes in PCSELs with different filling factors. For a filling factor of 10% and 15% either the degenerate B_1 and B_2 modes or the C mode is

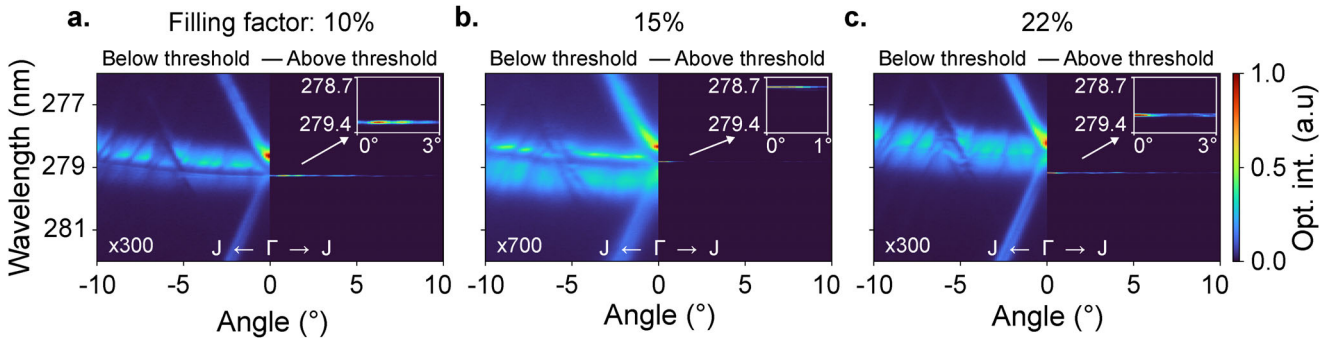

Figure 3. Measured angle-resolved emission spectra in linear scale in the Γ-J direction, below- and above threshold for PCSELs with hole-filling factors of a) 10%, b) 15%, and c) 22%. The left half of each figure was measured below threshold, the right half is above threshold. The multiplication factors at the bottom indicate how much the emission below threshold has been multiplied to be plotted in the same color scale as the measurements above threshold. The spectral and angular resolutions of the measurements are 17 pm and 0.12°, respectively. The insets show a zoomed-in angular-resolved spectrum of the lasing peak.

lasing, but it is difficult to experimentally determine which one is due to the very narrow wavelength spacing of these modes (caused by the small refractive index contrast between air and AlN) in relation to the spectral broadening of the dispersion branches. For the largest filling factor of 22%, the A mode clearly lases. Further insight into which mode lases and why is discussed in the Supporting Information where simulated results on loss rates and QW overlap factor for different filling factors are presented. The total loss (i.e., both lateral and vertical) is the lowest for the A mode for a filling factor of 22%, while it is the lowest for the B_1 mode for lower filling factors. In addition, the field overlap with the QW (and thereby the modal gain) is higher for the A mode for the largest filling factor. Thus, what is seen experimentally is likely a switch from the B_1 mode to the A mode at the higher filling factor of 22%.

2.4. Far-Field Emission Pattern

In **Figure** 4a–c, we show the far-field emission patterns of the three PCSELs discussed in Figure 3 when pumped at 1.2 times the lasing threshold (P_{th}). For the smallest filling factor we see six pairs of highly divergent dual emission lines at pump power densities above 12 MWcm^{-2}. Other PCSELs with similar filling factors (≈10%) show the same type of emission pattern, but sometimes only two or four of these pairs of dual emission lines appear, see Supporting Information. These types of far-fields indicate that the symmetry in the different crystallographic directions has been broken, either by the fabricated structure or the pump beam, and is in literature often referred to as 1D oscillations in PCSELs.[12,28,29] For this lowest filling factor (10%), the coupling between the propagating modes by the photonic crystal is weaker and therefore the influence from symmetry-breaking becomes more prominent. For the middle (15%) and highest filling factor (22%) on the other hand we see a doughnut-shaped far-field pattern in the center with a divergence angle of less than 1° at the FWHM; which is a characteristic feature of lasing in a PCSEL. Such a doughnut-shaped emission pattern has been reported for infrared PCSELs with circular holes[30,31] and is due to the circular symmetry of the holes leading to destructive interference at 0° resulting in zero intensity in the center of the far-field.[32]

For the highest filling factor, we can in addition see significant emission in certain well-defined directions up to very high far-field angles. These sixfold dual emission lines are compatible with the six-fold symmetry of the photonic crystal. A similar behavior has been observed in an infrared PCSEL[33] with a hexagonal lattice, where the dual emission lines coincided with a cross-section of the band structure of the B_2 band of the device at the lasing wavelength of the A mode. The same is true for our PCSEL with a hole-filling factor of 22%, see Figure 4e,f, where a cut through the B_2 band in the three-dimensional band structure at the lasing wavelength of the A mode is shown as well as a cut through the B_1 band. The latter would result in the smaller star-shaped pattern indicated by red in the simulated far-field, but even higher resolved far-field measurements would be required to investigate this further. What we in addition show here is that the dual emission lines have the same narrow emission wavelength as the doughnut-shaped emission in the center, see Supporting Information. This peculiar emission pattern is thus not caused by multi-mode lasing, but is rather due to a scattering of light from the lasing mode by for example small imperfections from material defects and etched-induced roughness (both enhanced at short wavelengths) or by a nonlinear scattering process such as four-wave mixing (enhanced by the high nonlinear susceptibility of AlN). For the middle filling factor of 15%, the PCSEL lases in the B_1 mode, and the dual emission lines are now much weaker. To better understand this behavior, we estimated the vertical and lateral losses in 80-μm-diameter devices with different filling factors using a k-space-weighted loss estimation applied to a band structure calculated by the guided mode expansion method (see Methods). For a 22% filling factor, the A mode has the lowest overall losses (276 ns^{-1}) and is therefore predicted to be the lasing mode, which is also the lasing mode we see experimentally. However, the vertical loss of the A mode (16 ns^{-1}) is relatively low; thus, a small amount of the power is coupled out vertically from this lasing mode. On the other hand, light scattered from the lasing A mode into the non-lasing B_2 band can easily be outcoupled into the vertical direction since the vertical loss of the B_2 band is comparatively high (429 ns^{-1}), see Supporting Information. Therefore, the emission seen in the far-field has a strong contribution from the light scattered into the non-lasing B_2 band. For a mid-range filling factor of 15%, the mode with the

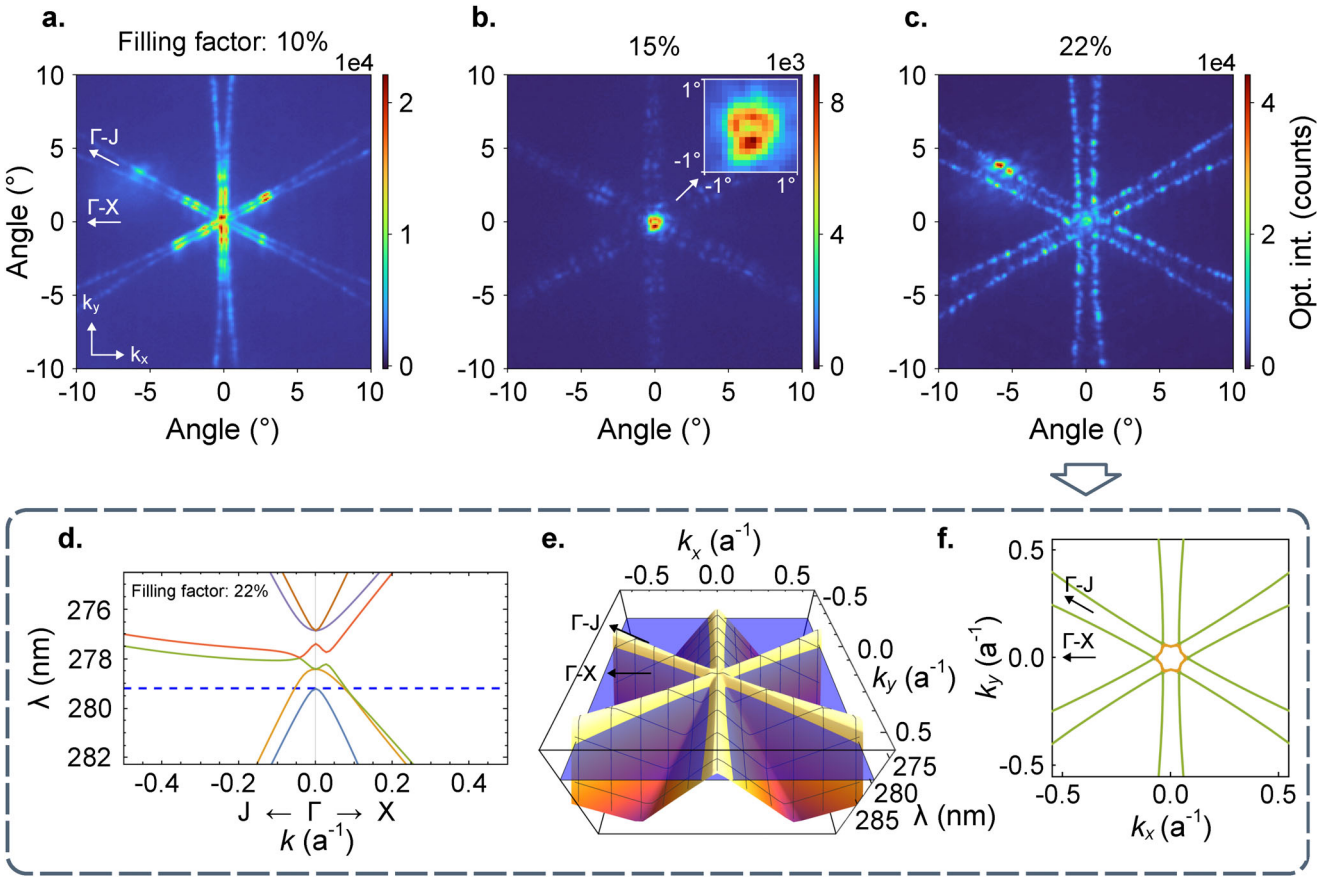

Figure 4. Measured far-field emission patterns of three PCSELs with hole-filling factors of a) 10%, b) 15%, and c) 22% when pumped at 1.2 × P_{th}. The inset in (b) depicts a zoomed-in image of the doughnut-shaped emission at the center. d) Simulated band structure for a filling factor of 22% showing all bands in Γ-X and Γ-J direction with a blue dotted line at the lasing wavelength. e) Simulated 2D band structure of band B_2 highlighting a cross-section of the band structure at the lasing wavelength (blue plane). f) Top-view of the same cross-section of mode B_2 (green) and a cross-section of mode B_1 (yellow) at the same lasing wavelength, corresponding to the top of the A band. The wave vectors k_x and k_y can be converted into angles in the x and y directions using the expression $\theta_{x,y} = \sin^{-1}(k_{x,y}/(2\pi n/\lambda_0))$, where n is the refractive index of the medium, λ_0 is the free-space wavelength.

overall lowest losses is instead the B_1 mode (234 ns^{-1}). The vertical loss of this mode is 184 ns^{-1}, which is comparable to that of the B_2 mode (183 ns^{-1}) at the same filling factor. Therefore, a significant portion of the power in this lasing mode is outcoupled and dominates the far-field emission, with only weak emission contribution coming from light scattered into the non-lasing B_2 band and vertically outcoupled.

The filling factor thus plays a vital role in controlling which mode will lase, which in turn determines the far-field emission pattern. A too small filling factor results in dominating 1D oscillation while a too large filling factor yields 2D oscillation, but with increased scattering losses and thereby a distorted far-field. However, with a filling factor in between, dominating 2D oscillation can be achieved with a high-quality and low-divergent far-field.

3. Conclusions

We here demonstrate the first optically pumped deep-UV PCSEL with emission wavelengths below 280 nm. It employs a hexagonal lattice with circular holes etched into the top AlN waveguide to improve the 2D coupling and lower the threshold. Under pulsed optical pumping, it shows single-mode emission with a doughnut-shaped far-field with a beam divergence of less than 1°. We also demonstrate the importance of choosing a proper filling factor for PCSELs in a low-refractive index material operating at short emission wavelengths. A too low filling factor results in dominating 1D oscillation, while a too high filling factor results in peculiar far-fields with the laser emission coupling into non-lasing bands, which distorts the far-field and produces large divergence emissions. By a proper choice of the filling factor, of about 15% in our devices, the desired 2D oscillation with high-quality far-fields with low beam divergence can be obtained. This holds great promise for the realization of high-power deep-UV lasers with high beam qualities.

4. Methods

Device Fabrication: The fabrication process of the optically pumped deep-UV PCSELs comprises three main steps: 1. e-beam lithography 2. development and 3. dry etching. For the e-beam lithography, the high-resolution e-beam resist hydrogen silsesquioxane (HSQ) with a thickness of 40 nm was used. After

the exposure, the resist was developed using the salty developer NaOH/NaCl for 120 s at room temperature. HSQ exhibited high dry etch resistance as it turns into SiO_x after e-beam exposure.[34] This SiO_x hard mask was used to etch the photonic crystal pattern 65 nm into the top AlN layer with a Cl_2/Ar dry etch, leaving 65 nm between the etched surface and the top QW. The remaining hard mask was then removed with buffered oxide etchant (BOE).

Experimental Setup and Characterization: The devices were characterized with an angular resolved spectrometer (Princeton Instruments SpectraPro HRS-750) and the experimental setup is illustrated in Figure S3 (Supporting Information). The devices were optically pumped from the photonic crystal side with a 266-nm pulsed laser (Alphalas PULSELAS-P, 20 kHz repetition rate, 0.55 ns pulse width) at room temperature with a pump beam spot size of 82 μm at full-width half-maximum. To measure the far-field emission pattern, all the emitted light was collected within the numerical aperture (NA = 0.39) of the objective (Thorlabs, LMU-20X-UVB). The pump beam was partially reflected by the sample toward the spectrometer. This light was filtered out by a long-pass filter. For the band structure measurements, where both spectral and angular information was needed simultaneously, the slit located at the entrance of the spectrometer was employed. The slit width was adjusted to only transmit the light within $\approx \pm 0.2$ degrees in one axis.

Device Simulation: For calculating the photonic band structure of an ideal PCSEL structure, two different approaches were used with different capabilities. First, the eigenfrequency solver (frequency domain module) with the FEM-solver in commercially-available simulation software COMSOL Multiphysics 6.1[35] was used in a 3D simulation to calculate the confinement factors for the different modes at the Γ-point for different filling factors, as well as the mode profile in Figure 1b and the band structure in Figure 1d.

The simulated structure corresponds to the fabricated PCSELs and included an AlN substrate, which also works as the bottom cladding, a 76-nm-thick $Al_{0.70}Ga_{0.30}N$ waveguide and a 100-nm-thick top AlN cladding. The 65-nm-thick upper part of the top cladding was the photonic crystal layer and included a hexagonal lattice of circular air holes with a lattice constant of 140 nm and variable radius. The QWs were included in the thickness of the waveguide layer but were not defined as layers with different refractive index, because the index difference between the QWs and barriers becomes reduced due to pumping of the QWs. A thickness of 250 nm for the substrate layer in this model was sufficient for realistic optical confinement. These simulations only use real refractive indices, i.e., no absorption or gain was considered. A refractive index of 2.260 was used for AlN and 2.418 for the $Al_{0.70}Ga_{0.30}N$ waveguide layer. The latter value had been fitted to obtain the measured wavelengths at the active band edges for different filling factors. The photonic band structure from this approach was used for estimating the optical losses for each mode, for calculating coupling coefficients, and to consider cross-sections through the band structure at specific wavelengths that form the dual emission lines in the far-field.

Loss Estimation: To estimate the vertical and lateral losses in a finite PCSEL it was crucial to consider finite-sized effects. The losses were estimated from the calculated photonic band structure, assuming a finite-sized pumped area with 80 μm in diameter. To calculate the band structure $\omega(k_x, k_y)$ was used the guided mode expansion method. In order to cover the whole first Brillouin zone, 40 different paths were defined from the Γ-point to the edge of the Brillouin zone, ranging between the Γ-J and Γ-X paths. On each path, 400 equidistant points were chosen to calculate the respective frequencies of all involved photonic bands. This covers one of twelve segments of the Brillouin zone, which was equal to all the other parts, as given by the symmetry of the lattice. The guided mode expansion was used to calculate the complex frequencies of each mode depending on the wave vector k in the vicinity of the Γ-point. The imaginary part of the frequency corresponds to the photon loss rate due to vertical outcoupling. To account for the finite size of the pumping spot, not only the Γ-point was considered (as for an infinitely large PCSEL), but the intensity distribution in k-space was assumed to follow a Gaussian distribution as follows:

$$I(k) \propto \exp\left[-\frac{k^2}{2\sigma_k^2}\right] \tag{1}$$

For a PCSEL diameter of 80 μm the width in k-space was $\sigma_k = \pi/80$ μm. To calculate the actual vertical outcoupling rate, the k-resolved vertical losses were averaged over the 2D k-space, weighted with the normalized mode intensity profile $I(k)$. This was done for each mode and for different filling factors. One notable difference in the band structures was the variation in outcoupling losses for different modes. Specifically, modes D_1 and D_2 exhibit high levels of radiation losses making it impossible to utilize these modes for lasing purposes. In contrast, mode A on the other hand showed very low outcoupling loss at the Γ-point indicating that the energy was efficiently confined in the structure and the mode may be favored for lasing. To estimate the lateral losses, the group velocity $v_{gr} = d\omega/dk$ was determined from the band structure for each point in 2D k-space near the Γ-point. Under the assumption that the photons leave the pumped region sideways with v_{gr} without scattering, the loss rate was approximated by v_{gr}/L, where L was the mean path length of a photon until the edge of the pumped region was reached. For this, the radius of the pumping spot, i. e., 40 μm was used. The resulting loss rates corresponding to each point in k-space were again averaged, weighted with the normalized mode intensity distribution $I(k)$, as for the vertical losses. Figure S7a (Supporting Information) shows a summary of the calculated vertical and lateral losses for six different transverse electric modes at three different hole-filling factors with the same labeling of the modes as for the band diagram in Figure 1d.

Supporting Information

Supporting Information is available from the Wiley Online Library or from the author.

Acknowledgements

This work was supported by Knut and Alice Wallenberg Foundation (Grant No: 2020.0119) and Leibniz Society within the SAW "UV SimTech" project (Contract no: K415/2021). The authors acknowledged Myfab for support and access to the nanofabrication laboratories at Chalmers University of Technology. The authors thank Niclas Lindvall and Marcus Rommel for

their help and support for the e-beam lithography system and the process, and Sylvia Hagedorn (FBH), and Markus Weyers (FBH) for providing AlN/sapphire substrates.

Conflict of Interest

The authors declare no conflict of interest.

Data Availability Statement

The data that support the findings of this study are available from the corresponding author upon reasonable request.

Keywords

AlGaN, filling factor, low divergence, photonic crystal surface-emitting laser (PCSEL), UV-C

Received: February 6, 2025
Revised: July 30, 2025
Published online: October 9, 2025

[1] N. N. Ledentsov, O. Y. Makarov, V. A. Shchukin, V. P. Kalosha, N. Ledentsov, L. Chrochos, M. B. Sanayeh, J. P. Turkiewicz, *J. Lightwave Technol.* **2022**, *40*, 1749.
[2] S. Wang, R. Ma, F. Cao, L. Luo, X. Li, *Sensors* **2024**, *24*, 1755.
[3] B. Fu, C. Zhang, W. Lyu, J. Sun, C. Shang, Y. Cheng, L. Xu, *Appl. Spectrosc. Rev.* **2020**, *57*, 112.
[4] L. A. Coldren, S. W. Corzine, M. L. Mašanovic, *Diode Lasers and Photonic Integr. Circuits*, John Wiley & Sons, Inc., New York **2012**.
[5] R. Michalzik, *VCSELs: Fundamentals, Technology and Applications of Vertical-Cavity Surface-Emitting Lasers*, Springer Berlin, Heidelberg, **2013**.
[6] S. Noda, T. Inoue, M. Yoshida, J. Gelleta, M. De Zoysa, K. Ishizak, *Adv. Opt. Photonics.* **2023**, *15*, 977.
[7] H.-Y. Lu, S.-C. Tian, C.-Z. Tong, L.-J. Wang, J.-M. Rong, C.-Y. Liu, H. Wang, S.-L. Shu, L.-J. Wang, *Light: Sci. Appl.* **2019**, *8*, 108.
[8] T. Inoue, M. Yoshida, J. Gelleta, K. Izumi, K. Yoshida, K. Ishizaki, M. De Zoysa, S. Noda, *Nat. Commun.* **2022**, *13*, 3262.
[9] M. Imada, S. Noda, A. Chutinan, T. Tokuda, M. Murata, G. Sasaki, *Appl. Phys. Lett.* **1999**, *75*, 316.
[10] M. Yoshida, S. Katsuno, T. Inoue, J. Gelleta, K. Izumi, M. D. Zoysa, K. Ishizaki, S. Noda, *Nature* **2023**, *618*, 727.
[11] H. Matsubara, S. Yoshimoto, H. Saito, Y. Jianglin, Y. Tanaka, S. Noda, *Science* **2008**, *319*, 445.
[12] K. Emoto, T. Koizumi, M. Hirose, M. Jutori, T. Inoue, K. Ishizaki, M. De Zoysa, H. Togawa, S. Noda, *Commun. Mater.* **2022**, *3*, 72.
[13] N. Taguchi, A. Iwai, M. Noguchi, H. Takahashi, A. Michiue, M. De Zoysa, T. Inoue, K. Ishizaki, S. Noda, *Appl. Phys. Express* **2024**, *17*, 1.
[14] Z. Zhang, M. Kushimoto, A. Yoshikawa, K. Aoto, L. J. Schowalter, C. Sasaoka, H. Amano, *Appl. Phys. Express* **2022**, *15*, 4.
[15] K. Sato, S. Yasue, K. Yamada, S. Tanaka, T. Omori, S. Ishizuka, S. Teramura, Y. Ogino, S. Iwayama, H. Miyake, M. Iwaya, T. Takeuchi, S. Kamiyama, I. Akasaki, *Appl. Phys. Express* **2020**, *13*, 3.
[16] F. Hjort, J. Enslin, M. Cobet, M. A. Bergmann, J. Gustavsson, T. Kolbe, A. Knauer, F. Nippert, I. Häusler, M. R. Wagner, T. Wernicke, M. Kneissl, Ă. Haglund, *ACS Photonics* **2021**, *8*, 135.
[17] Z. Zheng, Y. Mei, H. Long, J. Hoo, S. Guo, Q. Li, L. Ying, Z.-W. Zheng, B. Zhang, *IEEE Electron Device Lett.* **2021**, *42*, 375.
[18] E. Torres, J. Ciers, N. Rebelo, F. Hjort, M. A. Bergmann, S. Graupeter, J. Enslin, G. Cardinalli, T. Wernicke, M. Kneissl, Ă. Haglund, *Laser Photonics Rev.* **2025**, *18*, 2402203.
[19] S. Zhao, X. Liu, S. Y. Woo, J. Kang, G. A. Botton, Z. Mi, *Appl. Phys. Lett.* **2015**, *107*, 4.
[20] B. Le, X. Liu, N. H. Tran, S. Zhao, Z. Mi, *Opt. Express* **2019**, *27*, 5843.
[21] Z. Bian, X. Zhao, J. Liu, D. Kim, A. F. McKenzie, S. Thoms, P. Reynolds, N. D. Gerrard, A. S. M. Kyaw, J. Grant, K. Rae, J. R. Orchard, C. H. Hill, C. W. Munro, P. Ivanov, D. T. D. Childs, R. J. E. Taylor, R. A. Hogg, *npj Nanophotonics* **2024**, *1*, 13.
[22] S. Hagedorn, A. Mogilatenko, S. Walde, D. Pacak, J. Weinrich, C. Hartmann, M. Weyers, *Phys. Status Solidi B* **2021**, *258*, 10.
[23] J. G. Nedy, N. G. Young, K. M. Kelchner, Y. Hu, R. M. Farrell, S. Nakamura, S. P. DenBaars, C. Weisbuch, J. S. Speck, *Semicond. Sci. Technol.* **2015**, *30*, 8.
[24] M. Minami, S. Tomiya, K. Ishikawa, R. Matsumoto, S. Chen, M. Fukasawa, F. Uesawa, M. Sekine, M. Hori, T. Tatsumi, *Jpn. J. Appl. Phys.* **2011**, *50*, 8S1.
[25] S. Izumi, M. Minami, M. Kamada, T. Tatsumi, A. A. Yamaguchi, K. Ishikawa, M. Hori, S. Tomiya, *Jpn. J. Appl. Phys.* **2013**, *52*, 8S.
[26] S. Fan, J. D. Joannopoulos, *Phys. Rev. B* **2002**, *65*, 23.
[27] A. Kodigala, T. Lepetit, Q. Gu, B. Bahari, Y. Fainman, B. Kanté, *Nature* **2017**, *541*, 196.
[28] S. Kawashima, T. Kawashima, Y. Nagatomo, Y. Hori, H. Iwase, T. Uchida, K. Hoshino, A. Numata, M. Uchida, *Appl. Phys. Lett.* **2010**, *97*, 251112.
[29] G. Heliotis, R. Xia, D. D. C. Bradley, G. A. Turnbull, I. D. W. Samuel, P. Andrew, W. L. Barnes, *J. Appl. Phys.* **2004**, *96*, 6959.
[30] K. Sakai, E. Miyai, T. Sakaguchi, D. Ohnishi, T. Okano, S. Noda, *IEEE J. Sel. Areas Commun.* **2005**, *23*, 1335.
[31] Y. Liang, C. Peng, K. Sakai, S. Iwahashi, S. Noda, *Opt. Express* **2012**, *20*, 15945.
[32] E. Miyai, K. Sakai, T. Okano, W. Kunishi, D. Ohnishi, S. Noda, *Nature* **2006**, *441*, 946.
[33] Y. Kurosaka, K. Hirose, A. Watanabe, T. Sugiyama, Y. Liang, S. Noda, *Opt. Express* **2012**, *20*, 21773.
[34] H. Namatsu, Y. Takahashi, K. Yamazaki, T. Yamaguchi, M. Nagase, K. Kurihara, *J. Vac. Sci. Technol., B* **1998**, *16*, 69.
[35] COMSOL Multiphysics®v. 6.1, https://www.comsol.com, **2022**, COMSOL AB, Stockholm, Sweden.